

# Video-rate nanoscopy using sCMOS camera-specific single-molecule localization algorithms

Fang Huang<sup>1</sup>, Tobias M P Hartwich<sup>1–3,9</sup>, Felix E Rivera-Molina<sup>1,9</sup>, Yu Lin<sup>4,5</sup>, Whitney C Duim<sup>1</sup>, Jane J Long<sup>6</sup>, Pradeep D Uchil<sup>7</sup>, Jordan R Myers<sup>1</sup>, Michelle A Baird<sup>8</sup>, Walther Mothes<sup>7</sup>, Michael W Davidson<sup>8</sup>, Derek Toomre<sup>1</sup> & Joerg Bewersdorf<sup>1,4,5</sup>

**Newly developed scientific complementary metal-oxide semiconductor (sCMOS) cameras have the potential to dramatically accelerate data acquisition, enlarge the field of view and increase the effective quantum efficiency in single-molecule switching nanoscopy. However, sCMOS-intrinsic pixel-dependent readout noise substantially lowers the localization precision and introduces localization artifacts. We present algorithms that overcome these limitations and that provide unbiased, precise localization of single molecules at the theoretical limit. Using these in combination with a multi-emitter fitting algorithm, we demonstrate single-molecule localization super-resolution imaging at rates of up to 32 reconstructed images per second in fixed and living cells.**

Single-molecule switching nanoscopy (SMSN) techniques localize single molecules with precisions of ~10 nm by stochastically switching molecules on and off<sup>1–3</sup>. Thousands (or even tens of thousands) of camera frames of blinking subsets of molecules are typically recorded to obtain a single image at about 25- to 40-nm resolution. The temporal and spatial resolutions are limited by several factors: the number of photons emitted by a single molecule per frame and the sensitivity (quantum efficiency) and readout speed of the camera.

Back-illuminated electron-multiplying charge-coupled devices (EMCCDs) are commonly used for SMSN because of their low effective readout noise. However, the noise introduced by the amplification process results in a lower signal-to-noise ratio by a factor of  $\sim 2^{1/2}$  and effectively halves the high quantum efficiency (~95%) of these sensors to <48% (ref. 4) unless each pixel detects generally less than one photon on average<sup>5</sup>. Furthermore, the readout speed of  $512 \times 512$  pixel-EMCCD cameras is currently limited to 70 full frames per second (f.p.s.), and typical acquisition times for SMSN range from minutes to an hour. Since the first demonstration of live-cell imaging with these techniques<sup>6</sup>, an important goal has been to improve this speed. Limiting imaging

to smaller regions of interest (ROIs) of the chip or using cameras with fewer pixels can increase the frame rate to several hundred f.p.s. and allow live-cell SMSN of photoswitchable fluorescent proteins with a temporal resolution of several seconds, down to 500 ms with organic fluorophores<sup>7,8</sup>. However, the accessible field of view (FOV) is usually severely compromised for temporal resolutions of ~1 s.

This trade-off between imaging speed and FOV has substantially limited the capability of researchers using SMSN to address practical biological questions: many biological phenomena are so rare that imaging only small FOVs is highly inefficient, or the phenomena are best interpreted in the larger context of the cell (requiring imaging of large FOVs). This problem is of even greater concern when we consider the application of SMSN to high-throughput screening approaches. The trend toward systematic and quantitative analysis of cellular systems has not been expanded to nanoscopy, possibly because high recording speeds of large FOVs have been lacking, thus impeding the use of SMSN for systematic studies of complex cell biological processes.

Recently, sCMOS cameras have been introduced that feature an effective quantum efficiency of up to 73% at a wavelength of 600 nm, a large FOV (larger than  $2,000 \times 2,000$  pixels) and much faster readout speeds than those of EMCCD cameras—characteristics that make sCMOS devices attractive alternatives to EMCCD cameras. Unfortunately, sCMOS camera architecture results in every pixel having a unique noise characteristic, and the noise variances of individual pixels can range from several to thousands of analog-to-digital units squared (Fig. 1a and Supplementary Fig. 1).

The feasibility of SMSN using sCMOS cameras has been recently demonstrated<sup>9,10</sup>, but the non-negligible, pixel-dependent noise of sCMOS cameras makes the single-molecule localization algorithms originally designed for the Poisson-distributed and pixel-independent noise in EMCCD cameras<sup>4,11,12</sup> unable to provide reliable position estimates.

<sup>1</sup>Department of Cell Biology, Yale University School of Medicine, New Haven, Connecticut, USA. <sup>2</sup>Department of Biophysical Chemistry, University of Heidelberg, Heidelberg, Germany. <sup>3</sup>Department of New Materials and Biosystems, Max Planck Institute for Intelligent Systems, Stuttgart, Germany. <sup>4</sup>Department of Biomedical Engineering, Yale University, New Haven, Connecticut, USA. <sup>5</sup>Integrated Graduate Program in Physical and Engineering Biology, Yale University, New Haven, Connecticut, USA. <sup>6</sup>Yale College, Yale University, New Haven, Connecticut, USA. <sup>7</sup>Department of Microbial Pathogenesis, Yale University School of Medicine, New Haven, Connecticut, USA. <sup>8</sup>National High Magnetic Field Laboratory and Department of Biological Science, Florida State University, Tallahassee, Florida, USA. <sup>9</sup>These authors contributed equally to this work. Correspondence should be addressed to J.B. (joerg.bewersdorf@yale.edu).

RECEIVED 7 NOVEMBER 2012; ACCEPTED 22 APRIL 2013; PUBLISHED ONLINE 26 MAY 2013; DOI:10.1038/NMETH.2488

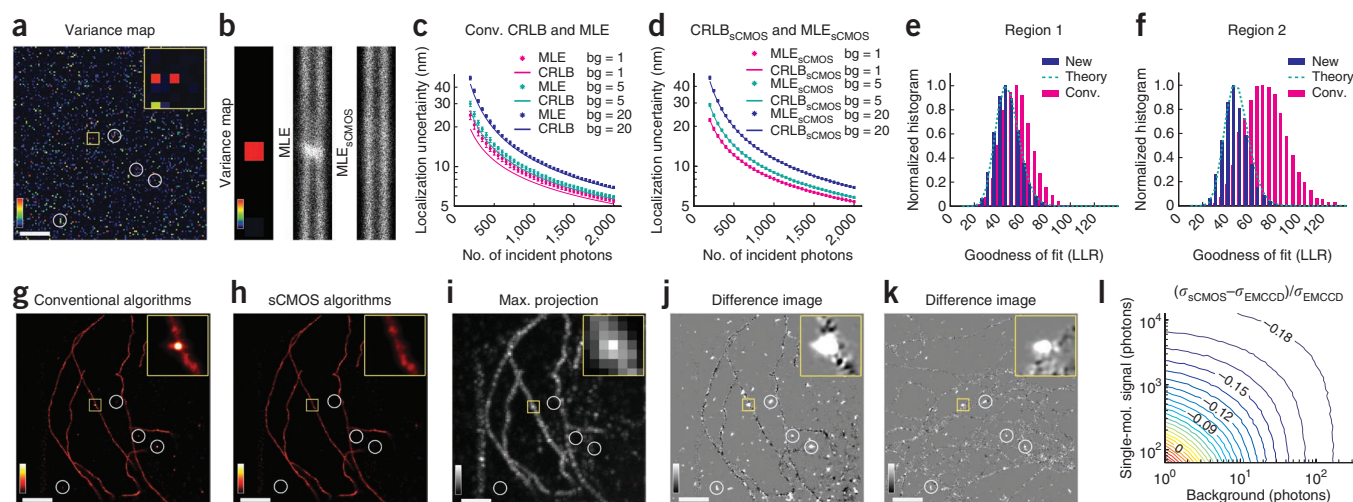


**Figure 1** | sCMOS camera-specific algorithms enable unbiased SMSN at the theoretical limit. **(a)** Readout variance map of a  $128 \times 128$ -pixel region in the center of a sCMOS camera. **(b)** Simulation of single emitters on a parallel line pair based on the shown variance map and localized using conventional MLE and  $\text{MLE}_{\text{sCMOS}}$ . **(c, d)** Uncertainty estimator performance comparison for sCMOS camera data between conventional MLE and CRLB **(c)** and between  $\text{MLE}_{\text{sCMOS}}$  and  $\text{CRLB}_{\text{sCMOS}}$  **(d)** for different detected background photon values per pixel ( $bg$ ) and single-molecule photon numbers incident on the camera chip. **(e, f)** Comparison of the goodness-of-fit log-likelihood ratio (LLR),  $\text{LLR}_{\text{sCMOS}}$  and theoretically predicted distribution for two different locations on the camera chip. **(g, h)** Reconstructed super-resolution images of microtubules analyzed using conventional **(g)** and sCMOS algorithms **(h)**. **(i)** Maximum projection of raw data used for **g, h** representing the diffraction-limited image. **(j)** Difference images of **g** and **h**. Zero differences are shown in gray. **(k)** Difference image of another microtubule data set recorded in the same camera region. Artifacts in **g, j, k** correlate with high-noise pixels in **a** as highlighted by the white circles. The yellow boxes in **a, g–k** denote the positions of the enlarged sections shown in the insets. **(l)** Relative improvement in localization precision ( $\sigma$ , s.d.) predicted by CRLB for EMCCD cameras and  $\text{CRLB}_{\text{sCMOS}}$  for a sCMOS camera, respectively. Color scales, bottom to top: 0–400  $\text{ADU}^2$ , where ADU = analog-to-digital units **(a, b)**; minimum-to-maximum signal **(i)**; same upper bound chosen for best visualization for **g, h**; same upper and lower bounds chosen for best visualization for **j, k**. Scale bars, 2  $\mu\text{m}$ .

Here we present algorithms that account for the intrinsic pixel-dependent readout noise of sCMOS cameras. We demonstrate artifact-free SMSN imaging of fixed and live specimens with sCMOS cameras at improved localization precision, high speed and large FOV.

## RESULTS

To illustrate the problem encountered when using conventional localization algorithms to analyze data from sCMOS cameras, we simulated recorded camera frames based on a test structure consisting of two parallel lines and included pixel-dependent variations in the readout noise and gain typical for sCMOS cameras (Fig. 1b and Online Methods). The simulated frames were then analyzed with a conventional maximum-likelihood estimation (MLE) algorithm, which has been demonstrated to perform at the Cramér-Rao lower bound (CRLB) limit with EMCCD data<sup>12</sup>. The two lines erroneously merged in the vicinity of a pixel with high readout noise (Fig. 1b), a result clearly demonstrating that the application of conventional localization methods can lead to inaccurate reconstructions when applied to sCMOS data sets.

We overcame this problem by applying a set of algorithms that included the observed noise behavior of sCMOS cameras in the localization process. This approach allowed unbiased and precise localization analysis with sCMOS cameras. In contrast to conventional localization methods, we modeled noise as a combined probability distribution of Poisson-distributed shot noise and Gaussian-distributed pixel-dependent readout noise. We consistently applied the noise model to all of the steps—image segmentation, single-molecule localization, fit rejection and uncertainty estimation—required for super-resolution analysis (Supplementary Fig. 2).

Accurate modeling of the pixel-dependent noise behavior requires quantification of the amplification gain, Gaussian noise variance, and offset of every pixel of the sCMOS camera. For this purpose, we carefully characterized our sCMOS camera (ORCA Flash 4.0, Hamamatsu Photonics) and determined the mean ('offset'), variance and amplification gain of each pixel (Online Methods, Fig. 1a and Supplementary Note).

With this information, unbiased and precise single-molecule localization analysis could be performed. In the first step, image segmentation, candidates for single-molecule localization were identified in the raw data. We adapted commonly used smoothing filters<sup>13</sup> for this purpose by statistically weighting the information from each pixel by its inherent variance and gain (Supplementary Note). This approach successfully eliminated large noise peaks in the smoothed images caused by noisy pixels, which could otherwise be interpreted as single molecules.

In the localization step following image segmentation, we estimated molecule positions for the identified candidates. Here, we implemented our sCMOS noise model in the likelihood function of the MLE framework (Supplementary Note). Consideration of the noise and gain inherent to each pixel requires that the likelihood function be based on a probability distribution described by the convolution of the Poisson-distributed photon shot noise with the pixel-dependent Gaussian noise distribution. This convolution must be computed for each pixel during every fitting iteration—a prohibitive step because of the overwhelming computational complexity. We solved this problem in our localization algorithm,  $\text{MLE}_{\text{sCMOS}}$ , by introducing an analytical approximation that greatly simplified the calculation while providing optimal accuracy and precision at the theoretical limit (Fig. 1c, d, Supplementary Fig. 3 and Supplementary Note).

To correctly identify and eliminate nonconverging fits and fit errors, we developed a goodness-of-fit test based on a log-likelihood ratio metric (**Supplementary Note**). Our algorithm,  $LLR_{sCMOS}$ , used the sCMOS camera noise model and its approximation introduced above. The metric followed a  $\chi^2$  distribution, as expected from theory, and thus allowed consistent and statistically well-defined fit rejection in spite of the strong pixel-noise and gain variations of sCMOS cameras (**Fig. 1e,f** and **Supplementary Note**).

Furthermore, to estimate the localization precision, we used our noise model to compute the CRLB, a commonly accepted estimation method of the localization uncertainty ( $CRLB_{sCMOS}$ ) (**Supplementary Note**).  $CRLB_{sCMOS}$  provided an accurate estimate of the localization uncertainty that was achieved by  $MLE_{sCMOS}$  (**Fig. 1c,d**).

We implemented all described sCMOS-specific algorithms in a highly parallelized graphical processor unit (GPU; GeForce GTX 690, Nvidia) environment using Compute Unified Device Architecture (CUDA, Nvidia), which shortened the analysis time by up to 2–3 orders of magnitude (**Supplementary Software**).

Application of  $MLE_{sCMOS}$  to the simulated sCMOS data set of two parallel lines described above eliminated the artifact observed with conventional algorithms (**Fig. 1b**). The contributions of high-noise pixels to the signal were statistically de-emphasized in the fitting process (**Supplementary Fig. 4**). This de-emphasis of a few sparse pixels did not substantially compromise the localization precision in the proximity of these pixels, as the signal from every emitter was spread over several pixels. In fact, our algorithm led to an improved localization performance because the influence of strong noise sources was suppressed (**Supplementary Fig. 4**), and the correct MLE was achieved because the appropriate statistics were considered for every pixel. As shown with simulated microtubule images (**Supplementary Fig. 5**) featuring relatively bright emitters (1,200 detected photons per emitter per frame), we obtained an approximately twofold resolution improvement with our new algorithms. Moreover, in contrast to conventional MLE,  $MLE_{sCMOS}$  achieved its theoretical lower bound of localization precision estimated by  $CRLB_{sCMOS}$  at all signal and background levels relevant for practical applications (**Fig. 1c,d**).

We observed the same phenomena with experimental data obtained by our custom-built microscope (**Supplementary Fig. 6** and Online Methods). We imaged microtubules in fixed COS-7 cells immunolabeled with Alexa Fluor 647 (Online Methods) and reconstructed super-resolution images. When we analyzed the data using conventional algorithms, we observed artifacts that were independent of the imaged sample but correlated with the distribution of high-noise pixels; our algorithms eliminated these errors (**Fig. 1g–k**).

Our algorithms allowed us to take advantage of the superior effective quantum efficiency, readout speed and FOV achievable with sCMOS cameras compared to those of EMCCD technology. Calculations based on the CRLB predicted that EMCCD cameras would achieve better localization precisions with below ~100 detected photons per emitter and negligible background noise (**Fig. 1l** and **Supplementary Fig. 7**), but for common experimental conditions the sCMOS camera we used would perform ~12–18% better. Analysis of images of a 100-nm-diameter fluorescent bead imaged with an EMCCD (Andor iXon 897)

and then with our sCMOS camera confirmed this prediction (**Supplementary Fig. 8** and Online Methods).

To demonstrate the versatility of our approach, we combined our algorithms with multi-emitter fitting analysis, which permits precise single-molecule localization at densities up to about tenfold higher than those normally achievable<sup>13</sup> (**Supplementary Note**). The corresponding reduction in the number of recorded frames combined with the high readout speed of sCMOS cameras allows substantially faster data acquisition.

We recorded a large-FOV ( $52 \times 52 \mu m^2$ ) super-resolution image of microtubules in COS-7 cells immunolabeled with Alexa Fluor 647 over 40 s at a frame rate of 400 f.p.s. ( $512 \times 512$  pixels). More than 4.4 million position estimates (corresponding to a density of ~2,700 estimates per micrometer of fiber length; individual molecules were detected for ~1.47 subsequent frames on average and localized with an average precision of ~14 nm; see Online Methods and **Supplementary Fig. 9**) resulted in a super-resolution image with approximately 30- to 40-nm resolution, which we confirmed by resolving the two opposite sides of a cylindrical microtubule filament (**Fig. 2a–c** and **Supplementary Data**). Recording a smaller,  $6.6 \times 6.6 \mu m^2$ -FOV ( $64 \times 64$ -pixel ROI) made it possible to increase the frame rate to 3,200 f.p.s. (**Fig. 2d–g**). When we applied multi-emitter fitting, a reliable super-resolution image could be obtained in only 33 ms, which corresponds to 106 recorded camera frames (**Fig. 2g**). The cost of this faster speed is a higher localization uncertainty compared to the data in **Figure 2a** (**Supplementary Fig. 9**). However, this frame rate represents a critical 15- to 90-fold speed improvement over previously reported values for high-speed SMSN<sup>7,8,14</sup>.

To further demonstrate the feasibility of our approach for high-content screening applications, we imaged the focal adhesion protein paxillin labeled with Alexa Fluor 647 in a ~ $26 \times 26 \mu m^2$  FOV ( $256 \times 256$  pixels) at a camera frame rate of 800 f.p.s. (**Supplementary Fig. 10**). In 3 s, a super-resolution image of the paxillin distribution could be recorded at a density of ~9,000 position estimates per  $\mu m^2$  (corresponding to an average of one position estimate per  $10.5 \times 10.5 nm^2$ ; individual molecules were detected for ~1.41 subsequent frames on average and localized with an average precision of ~22 nm; see Online Methods). Given a 1-s transition time to move the sample stage between positions, our technique has the potential to record nearly 1,000 different cells per hour and makes the prospect of screening cells by super-resolution imaging a possibility.

We demonstrated live-cell SMSN using clathrin-coated structures (CCSs), an established model system for nanoscopy<sup>7</sup>. We recorded raw data of clathrin light chain fused to the photoswitchable fluorescent protein mEos3.2 (ref. 15) on the lower surface of living HeLa cells (Online Methods) at 600 f.p.s. in a FOV of approximately  $26 \times 26 \mu m^2$  ( $256 \times 256$  pixels; individual molecules were detected for ~1.45 subsequent frames on average and localized with an average precision of ~22 nm; see Online Methods). A super-resolution image based on 34,800 camera frames accumulated in 58 s revealed expected ring-like structures of ~120–150 nm in diameter (**Supplementary Fig. 11**), representing the axial projection of clathrin-coated pits (CCPs). An elongated appearance of many of these structures was due to motion artifacts as revealed through color-coding of the localization estimates by their acquisition times (**Fig. 3a,b**). In contrast,



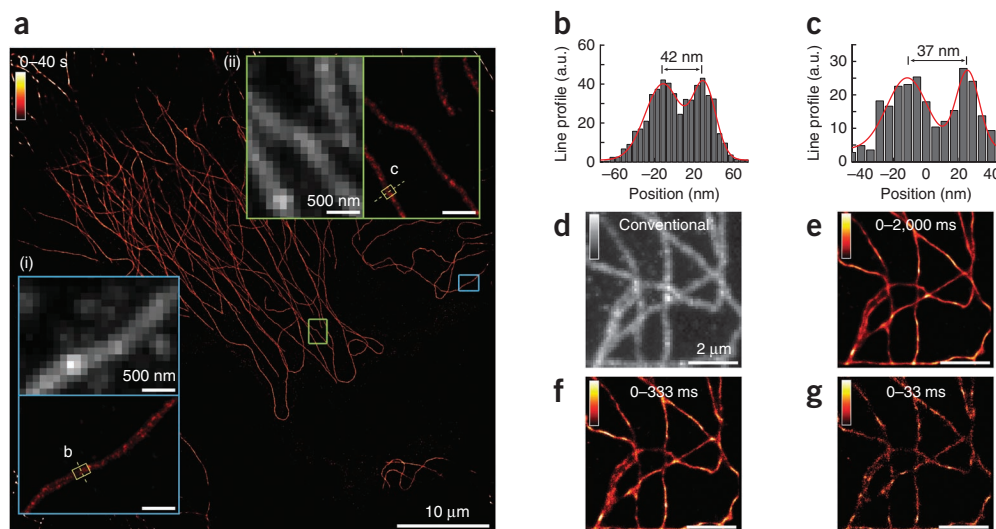


**Figure 2** | Unbiased, fast SMSN of fixed microtubules, demonstrating high-throughput capabilities. **(a)** Super-resolution image of microtubules in a  $53 \times 53\text{-}\mu\text{m}^2$  ROI imaged at 400 f.p.s. in 40 s. The data set was processed by the new sCMOS-specific algorithm resulting in about 4.4 million position estimates after filtering. The areas marked by the blue and green boxes are shown in the insets **(i)** and **(ii)** as maximum projections of the raw data (entire analyzed data set), representing the diffraction-limited wide-field images, and as super-resolution images. **(b,c)** Line profiles of position estimates in the small yellow boxes shown in **a**. **(d)** Maximum projection of a microtubule raw data set recorded in a  $6.5 \times 6.5\text{-}\mu\text{m}^2$  FOV at 3,200 f.p.s. in 2 s total. **(e–g)** Reconstructed super-resolution images obtained from different subsets of the same raw data stack using sCMOS-specific multi-emitter fitting. Color scales: minimum-to-maximum signal for all maximum-projection images, normalized to the same scale for super-resolution images in **a**, **i**, **ii** and for **e–g**. For visualization purposes, the upper bound in the color table has been adjusted for the overview image in **a**. a.u., arbitrary units.

data from only a 2-s time window confirmed that most clusters were indeed distributed in ring-like shapes (average localization estimates per CCP per 2-s time window:  $211 \pm 94$  s.d.,  $n = 32$ ; **Fig. 3c**). Displayed as movies (**Supplementary Videos 1–5**), these data showed the dynamic lateral motion of CCSs, including

fission-like events. Notably, the ring-shaped structures, indicative of CCPs or nearly completely formed vesicles, often moved in a directed manner at a speed of  $\sim 13\text{ nm s}^{-1}$ . One explanation for this phenomenon, as previously postulated on the basis of EM images<sup>16</sup>, is that growing actin filaments push CCSs away from their point of origin in the process of constriction and elongating the bud neck.

We expanded our studies to several other biological test-bed systems to show that sCMOS-based nanoscopy can be used to gain new insight about the dynamics of complexly shaped organelles, does not perturb cell function and can monitor fast dynamics.

To visualize mitochondrial dynamics, we imaged COS-7 cells expressing human pyruvate dehydrogenase  $\alpha 1$  (PDHA1) fused to tandem-dimer Eos (tdEos) (Online Methods). **Supplementary Video 6**, reconstructed at a speed of 2 f.p.s., shows the highly dynamic network and demonstrates the feasibility of sCMOS-based nanoscopy for imaging large, complex objects. Super-resolution imaging of EB3-mEos3.2 in living HeLa cells (Online Methods) showed the growth of

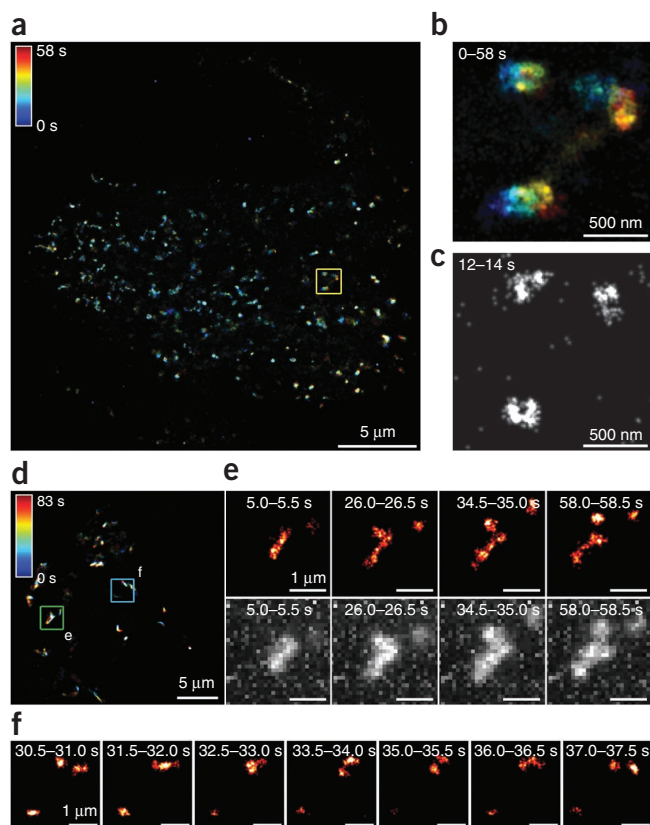


**Figure 3** | Live-cell SMSN at 0.5- to 2-s temporal resolution. **(a)** Super-resolution image of mEos3.2-labeled clathrin-coated pits (CCPs) in a live HeLa cell. The localization estimates are colored according to their recording time. **(b)** The enlarged image of the area marked by the yellow box in **a** reveals that movements of the structures over the course of recording obscure the details in the image. **(c)** Rings representing axial projections of CCPs can be resolved when only a 2-s time window of the data is displayed. **(d–f)** Peroxisome dynamics in a live COS-7 cell labeled by tdEos. **(d)** Overview image of an 83-s data set. Data have been colored as in **a**. **(e)** Super-resolution images (top) and maximum projections (bottom) of the raw data from the area in the green box in **d** in 0.5-s time intervals. **(f)** Super-resolution images at 0.5-s time resolution of the area highlighted by the blue box in **d**. See also **Supplementary Figure 11** and **Supplementary Videos 1–5** and **8**.

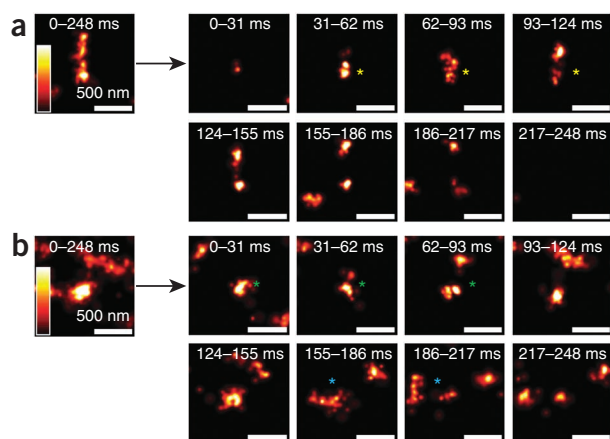


**Figure 4** | Video-rate live-cell nanoscopy of transferrin receptor clusters in live EA.hy926 cells. **(a,b)** Two examples of super-resolved transferrin cluster dynamics from a larger data set. Asterisks show splitting of single clusters into multiple clusters. Super-resolution imaging at a slower rate (about four super-resolution images per second; left) led to artifactual structures owing to diffusion as visualized by reconstructed sequences of the same data at higher frame rates ( $\sim 32$  super-resolution images per second; right). The upper bounds in the color table have been adjusted to the same values for the two 248-ms images and for all 31-ms images, respectively.

microtubule (+) ends at  $\sim 120 \text{ nm s}^{-1}$  (**Supplementary Fig. 12** and **Supplementary Video 7**), a result in good agreement with previously published values<sup>17</sup> and indicative that the laser light did not perturb microtubule polymerization. Additionally, we imaged peroxisome dynamics in COS-7 cells transfected with a peroxisomal membrane protein fused to tdEos (Online Methods). Imaging a FOV of approximately  $26 \times 26 \mu\text{m}^2$  at 600 f.p.s. and collecting the position estimates of 300 frames into single super-resolution images enabled us to record the dynamics of fusion and fission at a temporal resolution of two super-resolution images per second (**Fig. 3d–f** and **Supplementary Video 8**). Without substantial loss of signal, a time course of  $\sim 80 \text{ s}$  could be imaged corresponding to  $\sim 160$  reconstructed frames.

The temporal resolution achieved in these live-cell applications is several times higher than that of any other SMSN of fluorescent proteins previously reported<sup>6,7,18</sup> and matches the best reported temporal resolution for organic dyes, which are generally much brighter<sup>7</sup>.

Finally, we tested the speed limit of our live-cell imaging approach by using organic dyes and a small FOV to investigate transient clustering events of transferrin receptors on cell membranes<sup>19</sup>. Transferrin receptors labeled with transferrin–Alexa Fluor 647 (Online Methods) were imaged in a  $13 \times 13\text{-}\mu\text{m}^2$  FOV at an acquisition speed of 1,600 f.p.s. Super-resolution images were reconstructed from sequential sets of 50 frames corresponding to a 31-ms acquisition time, or 32 super-resolution images per second (**Fig. 4**, **Supplementary Videos 9** and **10** and **Supplementary Fig. 13**). Super-resolution images at a rate of four images per second failed to resolve fast events such as the transient nature of the receptor clustering and the dynamic movement of the clusters. Video-rate nanoscopy revealed that transferrin receptor cluster sizes are well below the diffraction limit. Additionally, the splitting of single clusters into multiple clusters indicated that the observed clusters consisted of multiple receptors.

## DISCUSSION

This method complements particle-tracking techniques, which can be substantially faster<sup>20</sup> but fail to work reliably at high particle densities and do not provide structural information such as the cluster size and shape. The imaging buffer for the Alexa Fluor 647 experiments and the high laser power may raise concerns about radical generation and cell damage during the imaging process. However, we did not observe any light-induced changes in cell morphology over the course of imaging in any of our live-cell experiments, a result in agreement with previous reports<sup>7</sup> (**Supplementary Note**). Long-term effects of SMSN on live samples remain to be investigated.

By accounting for pixel-dependent noise statistically, our algorithms allow unbiased single-molecule localization using sCMOS technology. They are applicable to any sCMOS sensor, including faster and more sensitive cameras being developed. Our algorithms can also be expanded to other detector arrays with nonuniform noise characteristics. The statistical basis of our algorithms is not restricted to particle localization and can be applied to the general field of quantitative image analysis.

The remaining foremost limitation for SMSN is the availability of fluorescent probes, labeling protocols and imaging buffers. Further optimization to increase the specificity of intracellular staining and the signal-to-background ratio in live-cell imaging will expand the application range. The recent progress in this area<sup>8,21–24</sup> makes future breakthroughs highly probable.

Although the data presented here have been obtained with only super-resolution microscopy, our method is equally applicable to single-particle tracking<sup>25</sup>. The previously achieved temporal resolution of 3.2 kHz in these techniques<sup>20</sup> could be improved sevenfold to  $\sim 20 \text{ kHz}$ . Moreover, methods relying on mapping multiple images onto the same camera chip for three-dimensional super-resolution<sup>26,27</sup> or multicolor imaging<sup>28,29</sup> can benefit from the sCMOS detector's larger FOV, higher quantum efficiency and increased frame rates while achieving localization accuracy and precision at the theoretical limit. The benefits of faster and more sensitive imaging of large FOVs pave the way for a new generation of high-throughput nanoscopes.

## METHODS

Methods and any associated references are available in the [online version of the paper](#).

*Note: Supplementary information is available in the online version of the paper.*

## ACKNOWLEDGMENTS

We thank J. Munro, P. Pellett, L. Schroeder, F. Bottanelli and M. Gudheti for helpful discussions about the buffer and sample preparation, J. Spatz for support, and P. de Camilli, O. Idevall-Hagren, T. Gould, E. Allgeyer and E. Kromann for helpful comments on the manuscript. We thank P. Xu (Chinese Academy of Sciences) for providing the mEos3.2 plasmid for initial experiments and G. Patterson (US National Institutes of Health) for the human clathrin light chain plasmid. This work was supported by grants from the Wellcome Trust (095927/A/11/Z), US National Institutes of Health (R01 CA098727 to W.M.) and Raymond and Beverly Sackler Institute for Biological, Physical and Engineering Sciences.

## AUTHOR CONTRIBUTIONS

F.H. and J.B. conceived the project. F.H., T.M.P.H., Y.L. and J.B. built the setup and designed the bead experiments. All authors designed the biological imaging experiments. F.H., T.M.P.H., Y.L., J.J.L., P.D.U. and J.R.M. performed the fixed-cell experiments. F.H., F.E.R.-M., W.C.D. and J.J.L. performed the live-cell experiments. M.A.B. and M.W.D. generated the mEos3.2 and tdEos plasmids. F.H. wrote the software and performed the simulations and analysis. All authors wrote the manuscript.

## COMPETING FINANCIAL INTERESTS

The authors declare competing financial interests: details are available in the online version of the paper.

Reprints and permissions information is available online at <http://www.nature.com/reprints/index.html>.

- Hell, S.W. Microscopy and its focal switch. *Nat. Methods* **6**, 24–32 (2009).
- Gould, T.J., Hess, S.T. & Bewersdorf, J. Optical nanoscopy: from acquisition to analysis. *Annu. Rev. Biomed. Eng.* **14**, 231–254 (2012).
- van de Linde, S., Heilemann, M. & Sauer, M. Live-cell super-resolution imaging with synthetic fluorophores. *Annu. Rev. Phys. Chem.* **63**, 519–540 (2012).
- Mortensen, K.I., Churchman, L.S., Spudich, J.A. & Flyvbjerg, H. Optimized localization analysis for single-molecule tracking and super-resolution microscopy. *Nat. Methods* **7**, 377–381 (2010).
- Chao, J., Ram, S., Ward, E.S. & Ober, R.J. Ultrahigh accuracy imaging modality for super-localization microscopy. *Nat. Methods* **10**, 335–338 (2013).
- Hess, S.T. *et al.* Dynamic clustered distribution of hemagglutinin resolved at 40 nm in living cell membranes discriminates between raft theories. *Proc. Natl. Acad. Sci. USA* **104**, 17370–17375 (2007).
- Jones, S.A., Shim, S.-H., He, J. & Zhuang, X. Fast, three-dimensional super-resolution imaging of live cells. *Nat. Methods* **8**, 499–505 (2011).
- Shim, S.-H. *et al.* Super-resolution fluorescence imaging of organelles in live cells with photoswitchable membrane probes. *Proc. Natl. Acad. Sci. USA* **109**, 13978–13983 (2012).
- Saurabh, S., Maji, S. & Bruchez, M.P. Evaluation of sCMOS cameras for detection and localization of single Cy5 molecules. *Opt. Express* **20**, 7338–7349 (2012).
- Long, F., Zeng, S. & Huang, Z.-L. Localization-based super-resolution microscopy with an sCMOS camera. Part II: experimental methodology for comparing sCMOS with EMCCD cameras. *Opt. Express* **20**, 17741–17759 (2012).
- Ober, R.J., Ram, S. & Ward, E.S. Localization accuracy in single-molecule microscopy. *Biophys. J.* **86**, 1185–1200 (2004).
- Smith, C.S., Joseph, N., Rieger, B. & Lidke, K.A. Fast, single-molecule localization that achieves theoretically minimum uncertainty. *Nat. Methods* **7**, 373–375 (2010).
- Huang, F., Schwartz, S.L., Byars, J.M. & Lidke, K.A. Simultaneous multiple-emitter fitting for single molecule super-resolution imaging. *Biomed. Opt. Express* **2**, 1377–1393 (2011).
- Zhu, L., Zhang, W., Elnatan, D. & Huang, B. Faster STORM using compressed sensing. *Nat. Methods* **9**, 721–723 (2012).
- Zhang, M. *et al.* Rational design of true monomeric and bright photoactivatable fluorescent proteins. *Nat. Methods* **9**, 727–729 (2012).
- Collins, A., Warrington, A., Taylor, K.A. & Svitkina, T. Structural organization of the actin cytoskeleton at sites of clathrin-mediated endocytosis. *Curr. Biol.* **21**, 1167–1175 (2011).
- Sironi, L. *et al.* Automatic quantification of microtubule dynamics enables RNAi-screening of new mitotic spindle regulators. *Cytoskeleton (Hoboken)* **68**, 266–278 (2011).
- Biteen, J.S., Goley, E.D., Shapiro, L. & Moerner, W.E. Three-dimensional super-resolution imaging of the midplane protein FtsZ in live *Caulobacter crescentus* cells using astigmatism. *ChemPhysChem* **13**, 1007–1012 (2012).
- Doherty, G.J. & McMahon, H.T. Mechanisms of endocytosis. *Annu. Rev. Biochem.* **78**, 857–902 (2009).
- Juette, M.F. & Bewersdorf, J. Three-dimensional tracking of single fluorescent particles with submillisecond temporal resolution. *Nano Lett.* **10**, 4657–4663 (2010).
- Lukinavičius, G. *et al.* A near-infrared fluorophore for live-cell super-resolution microscopy of cellular proteins. *Nat. Chem.* **5**, 132–139 (2013).
- Benke, A. & Manley, S. Live-cell dSTORM of cellular DNA based on direct DNA labeling. *ChemBioChem* **13**, 298–301 (2012).
- Vaughan, J.C., Jia, S. & Zhuang, X. Ultrabright photoactivatable fluorophores created by reductive caging. *Nat. Methods* **9**, 1181–1184 (2012).
- Lee, M.K., Williams, J., Twieg, R.J., Rao, J. & Moerner, W.E. Enzymatic activation of nitro-aryl fluorogens in live bacterial cells for enzymatic turnover-activated localization microscopy. *Chem. Sci.* **4**, 220–225 (2013).
- Manley, S. *et al.* High-density mapping of single-molecule trajectories with photoactivated localization microscopy. *Nat. Methods* **5**, 155–157 (2008).
- Juette, M.F. *et al.* Three-dimensional sub-100 nm resolution fluorescence microscopy of thick samples. *Nat. Methods* **5**, 527–529 (2008).
- Aquino, D. *et al.* Two-color nanoscopy of three-dimensional volumes by 4Pi detection of stochastically switched fluorophores. *Nat. Methods* **8**, 353–359 (2011).
- Testa, I. *et al.* Multicolor fluorescence nanoscopy in fixed and living cells by exciting conventional fluorophores with a single wavelength. *Biophys. J.* **99**, 2686–2694 (2010).
- Gunewardene, M.S. *et al.* Superresolution imaging of multiple fluorescent proteins with highly overlapping emission spectra in living cells. *Biophys. J.* **101**, 1522–1528 (2011).



## ONLINE METHODS

**Camera variance, gain and offset calibration.** We recorded a series of dark images (60,000 frames) with our sCMOS camera (ORCA-Flash 4.0, Hamamatsu Photonics). The automatic pixel correction that is offered by many sCMOS camera models was disabled for all calibration and application measurements to avoid automatic replacement of high-variance pixels by the average of the neighboring pixels. This correction otherwise prevents correct statistical treatment of the pixel signal. The mean ('offset'),  $\sigma_i$ , and the variance,  $\text{var}_i$ , for each pixel  $i$  were calculated by temporal mean and variance operations over the acquired dark frames. The amplification gain,  $g_i$ , for each pixel was estimated from 15 sets of 20,000 frames each that were recorded at different illumination intensities ranging from approximately 20 to 200 photons per pixel (**Supplementary Note**).

**Simulations of super-resolution sCMOS data sets.** For the simulated line pattern, single emitters were simulated using a pixel-integrated symmetric two-dimensional (2D) Gaussian model<sup>13</sup>. The switching behavior was simulated using a Markov model with  $k_{\text{off}}$  (bright-to-dark) and  $k_{\text{on}}$  (dark-to-bright) rates of 0.8 frame<sup>-1</sup> and 10<sup>-5</sup> frame<sup>-1</sup>, respectively. These rates were chosen to ensure nonoverlapping emitters. Single emitters were simulated with 200 photons per molecule incident on the camera, 5 photons detected per pixel as the background, a 2D Gaussian-shaped point-spread function (PSF) with 133-nm s.d., 75% camera quantum efficiency and a pixel size of 103 nm to match our experimental setup. Images of the simulated structure of two lines with 80-nm distance were first generated with Poisson noise, and then pixel-dependent Gaussian noise was added to each pixel in the simulated subregion where the variance, offset and gain values of each pixel had been obtained from a physical subregion of our sCMOS camera. This noise mapping method ensures realistic simulation of sCMOS noise behavior.

**Generation of goodness-of-fit-metric (LLR) histograms.** For **Figure 1e,f**, we simulated 10,000 7 × 7-pixel subregions each with a single emitter (200 total incident photons per single molecule and 5 background photons per pixel) separately in two different subregions. Noise was added to the images using the noise mapping method described above. Localization analysis was performed using MLE and MLE<sub>sCMOS</sub>, respectively, and LLR and LLR<sub>sCMOS</sub> were calculated. The  $\chi^2$  distribution with 45 degrees of freedom (number of pixels – number of fit parameters) (ref. 30) is plotted in **Figure 1e,f**.

**Comparison of MLE results with CRLB.** For **Figure 1c,d**, at each incident photon level, simulations were performed at 1,000 randomly distributed positions using the noise mapping method. In each subregion, 1,000 single emitters were simulated and fit by MLE and MLE<sub>sCMOS</sub>, respectively. The localization uncertainty is the s.d. of the localization estimates. The distribution of these values over the 1,000 subregions then provides a mean localization uncertainty and its s.d. The CRLB and CRLB<sub>sCMOS</sub> were determined as the mean value of the CRLBs calculated from the localization estimates of all 1,000 × 1,000 simulations for each signal photon-background combination for the conventional method and sCMOS method, respectively.

**Imaging of fluorescent beads and single-molecule analysis.** A sample of 100-nm fluorescent beads (F-8801, Life Technologies) was prepared on a coverslip and imaged with our custom-built microscope (**Supplementary Fig. 6**) using a 63×/1.2-NA water-immersion objective (C-Apochromat 63×/1.2 W Corr, Zeiss). The effective pixel sizes were matched between the two cameras for fair comparison using relay lenses (pixel size in the sample plane: 101 nm for EMCCD and 103 nm for sCMOS). A mirror on a magnetic retention base enabled fast switching between the two cameras with minimal disturbance to the imaging system. A 568-nm laser (Innova 300, Coherent) was used at a low intensity (~0.1 mW measured before the objective) as the excitation source. Images were taken first with the EMCCD and then with the sCMOS camera to rule out a decrease in localization precision caused by photobleaching. Photobleaching was not observed over the acquisition period (data not shown). Data sets from EMCCD and sCMOS data sets (800 frames each), were analyzed using MLE<sup>12</sup> and MLE<sub>sCMOS</sub> (**Supplementary Note**), respectively.

**Plasmid construction.** The Human paxillin sequence (NM\_002859.2) was amplified using PCR and cloned into the pCMV-3TAG 1A vector (Agilent Technologies) to obtain a construct expressing an N-terminal Flag-tagged version of paxillin.

mEos3.2 and tdEos fluorescent protein (FP) expression vectors were constructed using C1 and N1 (Clontech-style) cloning vectors. The FP cDNAs were amplified with a 5' primer encoding an AgeI site and a 3' primer encoding a NotI site (N1) or a BspEI site (C1) for insertion into the appropriate cloning vector backbone. The PCR products and EGFP-C1 and EGFP-N1 cloning vectors were gel purified and digested with the appropriate enzymes before ligation to generate new cloning vectors with the Eos FP coding regions. All fusions were first constructed using an EGFP variant with mutations designed to enhance folding (mEmerald), which is well behaved with respect to monomeric character and lack of localization artifacts. These vectors served as pilots to demonstrate proper localization of constructs to confirm the performance of the photoconvertible FPs. Thus, an N-terminal fusion (with respect to the targeting protein) was constructed to produce a human clathrin light chain (CLC) fusion (NM\_001834.2; gift from G. Patterson, NIH) with a 15-amino-acid linker separating the fluorescent protein from clathrin. CLC cDNA was amplified using the primers listed in **Supplementary Table 1**. The resulting PCR product and mEmerald-C1 cloning vector were digested with the appropriate restriction enzymes, and the products were ligated to yield mEmerald-CLC. The same process was also used to generate human EB3 (NM\_012326.2; OriGene) using the primers in **Supplementary Table 1**. The PCR product and mEmerald-C1 were digested by the appropriate enzymes and ligated to yield mEmerald-EB3 with an 18-amino-acid linker separating the proteins. In both cases, after proper localization was confirmed, mEos3.2 was substituted for mEmerald through digestion with BglII and NheI enzymes. This yielded mEos3.2-CLC and mEos3.2-EB3.

To produce a pilot C-terminal fusion (with respect to the targeting protein), human peroxisomal membrane protein (PMP) (NM\_018663.1; OriGene) was amplified using the primers in **Supplementary Table 1**. The resulting PCR product and mEmerald-N1 were digested by the appropriate restriction

enzymes, and the products were ligated to yield PMP-mEmerald with a 10-amino-acid linker separating the proteins. After confirmation of proper localization, the resulting construct and tdEos-N1 were then sequentially digested with AgeI and NotI and ligated to form PMP-tdEos.

In a similar manner, human pyruvate dehydrogenase alpha 1 (PDHA1) (NM\_000284.3; OriGene) was amplified using the primers listed in **Supplementary Table 1**. The PCR product and mEmerald-N1 were digested by the appropriate enzymes and ligated to yield PDHA1-mEmerald with a 10-amino-acid linker separating the proteins. After we confirmed the proper localization, the resulting construct and tdEos-N1 were then digested with BamHI and NotI and ligated together to form PDHA1-tdEos.

The DNA used for transfection was prepared using the Plasmid Maxi kit (Qiagen). To ensure proper localization, mEos3.2 and tdEos fusion proteins were characterized by transfection in HeLa cells (CCL2 line; ATCC) using Effectene (Qiagen) and ~1 µg vector. Transfected cells were grown on coverslips in DMEM/F12, fixed after 48 h, and mounted with gelvatol.

**Sample preparation for microtubule imaging.** COS-7 cells (ATCC) were grown in DMEM/F12 (Invitrogen) supplemented with 2 mM L-glutamine (Gibco), 10% fetal bovine serum (FBS, ATCC) and 1% penicillin (10,000 IU/mL)/streptomycin (10,000 µg/mL) (P/S, ATCC) at 37 °C with 5% CO<sub>2</sub>. Prior to imaging, cells were grown in 35-mm dishes on no. 1.5 glass coverslips precoated with poly(L-lysine) (MatTek) and fibronectin. For microtubule labeling, cells were washed three times with PBS prewarmed to 37 °C and were pre-extracted with 0.2% saponin (Sigma) in cytoskeleton buffer (CSB, 10 mM MES pH 6.1 (Sigma), 150 mM NaCl, 5 mM MgCl<sub>2</sub> (Sigma), 5 mM EGTA (Sigma), 5 mM glucose) for 1 min at room temperature. After the solution was aspirated, the cells were fixed with 3% paraformaldehyde (PFA, Electron Microscopy Sciences) and 0.1% glutaraldehyde (Electron Microscopy Sciences) diluted in CBS for 15 min. Cells were washed three times for 3-min intervals with PBS and then permeabilized and blocked with blocking buffer (3% BSA (Sigma) and 0.2% TX-100 in PBS) for 30 min while gently rocking. The buffer was aspirated, and the cells were incubated with mouse monoclonal anti-α-tubulin antibody (Sigma T5168, 1:1,000 dilution) at room temperature for 1 h. Cells were washed three times for 3-min intervals using wash buffer (WB; 0.05% TX-100 in PBS) and incubated with Alexa Fluor 647 goat anti-mouse IgG (Invitrogen A-21236) at a concentration of approximately 5 µg/mL for 1 h. Cells were washed with the WB for three 3-min intervals and postfixed with 3% PFA and 0.1% glutaraldehyde diluted in CSB for 10 min. Samples were washed three times in PBS for 3-min intervals and stored in PBS at 4 °C until imaging.

**Sample preparation for focal adhesion imaging.** We seeded  $2 \times 10^5$  HeLa cells grown in DMEM (Invitrogen) with 10% FBS on a 35-mm glass-bottom dish (MatTek; no. 1.5 coverglass). After overnight incubation, the cells were transfected with 500 ng of plasmid DNA expressing N-terminal Flag-tagged focal adhesion marker paxillin using FuGENE HD transfection reagent (Promega; E2311). The cells were fixed 24 h after transfection with 4% PFA and were processed for immunofluorescence. Briefly, the cells were permeabilized with 0.5% Triton X-100, treated with monoclonal antibodies to the Flag epitope (1:1,000

dilution, Clone M2, Sigma-Aldrich; F3165; 1 mg/mL) in PBS containing 3% bovine serum albumin fraction V (American Bioanalytical; AB01088). This was followed by treatment with Alexa Fluor 647-conjugated goat secondary antibodies against mouse (1:2,000 dilution; Invitrogen; A-21236; 2 mg/mL). The cells were then postfixed with 4% PFA. Immediately before image acquisition, the cells were mounted in STORM-imaging buffer and overlaid with mineral oil.

**Sample preparation for live-cell imaging with photoswitchable fluorescent proteins.** HeLa and COS-7 cells grown in DMEM (high glucose, phenol red-free; Invitrogen) supplemented with 10% FBS and 1% P/S were seeded on a 35-mm glass-bottom dish (MatTek; no. 1.5 coverglass). After overnight incubation, the cells were transfected with 2 µg of plasmids using FuGENE HD transfection reagent (Promega). Cells were washed with supplemented medium 24 h post-transfection and were incubated overnight. Before imaging, the cells were washed with supplemented growing medium.

**Sample preparation for live-cell imaging of transferrin.** EA.hy926 cells were grown in DMEM (high glucose, phenol red-free, Invitrogen) supplemented with 10% FBS and 1% P/S at 37 °C with 5% CO<sub>2</sub>. Prior to imaging, cells were grown in 35-mm dishes with no. 1.5 glass coverslips coated with collagen (MatTek). One hour before labeling, EA.hy926 cells were incubated in DMEM (high glucose, phenol red-free) without serum. Transferrin from human serum, conjugated to Alexa Fluor 647 (Life Technologies), was reconstituted with deionized water to a concentration of 5 mg/mL and stored at 4 °C. The transferrin-Alexa Fluor 647 conjugate was diluted to 10 µg/mL in DMEM (high glucose, phenol red-free) and incubated with EA.hy926 cells for 45 min. After labeling, cells were washed three times with 1× PBS. To remove transferrin-Alexa Fluor 647 bound to the plasma membrane, cells were washed once with 50 mM MES, pH 5.0, 150 mM NaCl and twice with 1× PBS. Cells were imaged in 1 mL of DMEM (high glucose, phenol red-free) supplemented with 25 µM 2-ME, 10 µL of glucose oxidase and 4 µL of catalase at room temperature.

**Imaging buffer preparation for Alexa Fluor 647-labeled samples.** Oxygen-scavenging enzymes, catalase from bovine liver (Sigma C40) and glucose oxidase from *Aspergillus niger* (Sigma G2133), were reconstituted in 20 mM Tris pH 7.4 (Sigma), 50 mM NaCl (Sigma) and 28.4 mM 2-mercaptoethanol (2-ME, Sigma). Oxygen scavenging enzymes were stored separately in 50% glycerol at -20 °C at concentrations of 500 kU/mL of catalase and 13.5 kU/mL of glucose oxidase. Oxygen-scavenging enzymes were diluted into imaging buffer (50 mM Tris, pH 8.0, 50 mM NaCl (Sigma), 10% glucose) immediately before use. For imaging, 20 µL of glucose oxidase and 4 µL of catalase stocks were added to 1 mL of 1% (v/v) 2-ME in imaging buffer.

**Imaging of fixed and live cells.** All biological images were recorded on a custom-built setup (**Supplementary Fig. 6**) based on a commercial microscope stand (Axio Observer D1, Carl Zeiss MicroImaging) with a 100×/1.46-NA oil-immersion objective (alpha Plan-Apochromat 100×/1.46 oil, Zeiss). The setup is equipped with lasers emitting at 405 nm (CrystaLaser, 50 mW), 568 nm (Coherent Innova 300, ~400 mW) and 642 nm



(MPB Communications, 500 mW). Fluorescence was recorded by our sCMOS camera through the side port of the stand. All data were recorded at room temperature.

Fixed microtubule structures were imaged in a  $128 \times 128$ -pixel ROI for 40,000 frames at 1,600 f.p.s. (Fig. 1g–k), a  $512 \times 512$ -pixel ROI for 16,000 frames at 400 f.p.s. (Fig. 2a) and a  $64 \times 64$ -pixel ROI for 30,000 frames at 3,200 f.p.s. (Fig. 2d–g). The 642-nm laser was used at average intensities of  $\sim 18 \text{ kW/cm}^2$ ,  $\sim 6 \text{ kW/cm}^2$  and  $\sim 7 \text{ kW/cm}^2$ , respectively. Images were acquired using HCImage software (Hamamatsu). Focal adhesions were recorded in a  $256 \times 256$ -pixel ROI for 2,400 frames at 800 f.p.s. with the 642-nm average laser intensity set to  $\sim 9 \text{ kW/cm}^2$ . Clathrin data were recorded in a  $256 \times 256$ -pixel ROI for 50,000 frames at 600 f.p.s. with the 568-nm average laser intensity set to  $\sim 5 \text{ kW/cm}^2$ . Mitochondria were recorded in a  $256 \times 256$ -pixel ROI for 80,000 frames at 400 f.p.s. with the 568-nm average laser intensity set to  $\sim 5 \text{ kW/cm}^2$ . EB3 data were recorded in a  $256 \times 256$ -pixel ROI for 30,000 frames at 600 f.p.s. with the 568-nm average laser intensity set to  $\sim 5 \text{ kW/cm}^2$ . Peroxisomes were recorded in a  $256 \times 256$ -pixel ROI for 50,000 frames at 600 f.p.s. with the 568-nm average laser intensity set to  $\sim 5 \text{ kW/cm}^2$ . Transferrin data were recorded in a  $128 \times 128$ -pixel ROI at 1,600 f.p.s. with the 642-nm average laser intensity set to  $\sim 7 \text{ kW/cm}^2$ . During imaging, the intensity of the 405-nm activation laser was manually increased from 0 to  $0.3 \text{ W/cm}^2$  (for a  $512 \times 512$ -pixel ROI) and from 0 to  $1.8 \text{ W/cm}^2$  (for  $256 \times 256$ -,  $128 \times 128$ - and  $64 \times 64$ -pixel ROIs) to ensure optimal particle densities for either single-emitter fitting or multi-emitter fitting<sup>31</sup>.

**Super-resolution analysis and reconstruction for fixed- and live-cell experiments.** For the conventional MLE method, raw images recorded with the sCMOS camera were first Poisson calibrated<sup>13</sup> by subtracting a predetermined offset value and then dividing by a constant gain factor (provided by the manufacturer)<sup>13,32</sup>. The calibrated images were then analyzed using the conventional MLE method. The fit parameters were the emitter position ( $x, y$ ), the number of detected photons and the background value. The localization precision was estimated by the conventional CRLB. Finally, super-resolution images were reconstructed by plotting pixel-integrated 2D Gaussians<sup>13</sup> at each localized position, each with s.d. in the  $x$  and  $y$  directions equal to the corresponding CRLB estimates of localization uncertainties.

For the sCMOS-specific method, particles were identified and segmented in the raw sCMOS images using the sCMOS-specific image-segmentation algorithm (Supplementary Note) and then fitted using  $\text{MLE}_{\text{sCMOS}}$ . The localization precision was estimated by  $\text{CRLB}_{\text{sCMOS}}$ . Super-resolution images for Figure 1 were reconstructed as described above for conventional MLE.

To obtain the super-resolution images shown in Figures 2–4, only the sCMOS-specific algorithms were used. In Figures 2a and 3, single-emitter analysis was performed and localization results were filtered using  $\text{LLR}_{\text{sCMOS}}$ . For reconstruction, localization estimates were binned into a 2D histogram image. The value of each pixel indicates the number of localization estimates in the pixel. The pixel sizes in the 2D histogram images shown were 5.15 nm in Figure 2a, 10.3 nm in Figure 3a–c and 20.6 nm in Figure 3d–f.

To aid visualization, each image was convolved with a 2D Gaussian kernel with s.d.  $\sigma = 1.5$  pixels (Fig. 2a) or 1 pixel (Fig. 3).

In Figures 2d–g and 4, multi-emitter fitting was performed using the following fitting parameters: position ( $x, y$ ), effective photon count and background. Initial guesses of effective photon count were 250 (Fig. 2d–g) and 200 (Fig. 4). For all data sets, the maximal number of emitter models fitted within a single sub-region was set to 4 and  $\sigma$  of the Gaussian emitter model was set to 133 nm. A  $P$  value of  $10^{-10}$  from the  $\text{LLR}_{\text{sCMOS}}$  was used as the rejection threshold. To reconstruct the super-resolution image, localization estimates from the remaining particles were binned into a 2D histogram image with 10.3-nm pixel size. To aid visualization, each resulting image was convolved with a 2D Gaussian kernel with  $\sigma = 1$  pixel (Fig. 2e–g) or 2 pixels (Fig. 4).

To provide an estimate for the average number of consecutive frames over which single molecules were detected, we considered localization events to stem from the same molecule if they were located within a radius of three times the localization uncertainty.

**Generation of difference images.** For Figure 1j,k, after localization using MLE or  $\text{MLE}_{\text{sCMOS}}$ , 2D histogram images were generated with 10.3-nm pixel size. The difference image was obtained by subtracting the  $\text{MLE}_{\text{sCMOS}}$  image from the conventional MLE image. To aid visualization, the resulting images were convolved with a 2D Gaussian kernel ( $\sigma = 2$  pixels).

**Tracking of EB3 and clathrin-coated pits.** The series of EB3 super-resolution images was imported in Velocity 6.2 (Velocity Medical Solutions), and the tips of the growing microtubules were tracked using the manual tracking mode. For the series of super-resolution CCP images, the centers of identified CCPs were tracked manually in Matlab during the individual periods of directed movement (5–20 s).

**Emitter density calculation.** To estimate the number of localized emitters per area in Figure 2 and Supplementary Figure 10, we extracted the number of localization estimates from a representative 1- $\mu\text{m}$  segment of straight microtubule using an integration width of 80 nm (Fig. 2a). For the paxillin data, estimates were counted in a  $240 \text{ nm} \times 240 \text{ nm}$  box centered on a large focal adhesion (Supplementary Fig. 10a). The 1D and 2D localization densities were calculated as the number of localization estimators determined per length unit and per area unit, respectively.

**Nyquist resolution measurement.** To estimate the Nyquist resolution in Figure 4a,b, we first determined masks covering the area of each transferrin cluster in each super-resolution image. Determining the number of localization estimates in the clusters and dividing it by the cluster area yielded the localization density. The Nyquist resolution was calculated for the 2D case<sup>7</sup> as  $2/(\text{localization density})^{1/2}$ .

30. Wilks, S.S. The large-sample distribution of the likelihood ratio for testing composite hypotheses. *Ann. Math. Stat.* **9**, 60–62 (1938).

31. Shore, E. & Small, A. Optimal acquisition scheme for subwavelength localization microscopy of bleachable fluorophores. *A. Opt. Lett.* **36**, 289–291 (2011).

32. Lidke, K.A., Rieger, B., Lidke, D.S. & Jovin, T.M. The role of photon statistics in fluorescence anisotropy imaging. *IEEE Trans. Image Process.* **14**, 1237–1245 (2005).